nature COMMUNICATIONS

ARTICLE

DOI: 10.1038/s41467-018-02907-8 OPEN

Competition between electron pairing and phase coherence in superconducting interfaces

G. Singh[1,2], A. Jouan[1,2], L. Benfatto[3,4], F. Couëdo[1,2], P. Kumar[5], A. Dogra[5], R.C. Budhani[6], S. Caprara[3,4] M. Grilli[3,4], E. Lesne[7], A. Barthélémy[7], M. Bibes[7], C. Feuillet-Palma[1,2], J. Lesueur[1,2] & N. Bergeal[1,2]

In $LaAlO_3/SrTiO_3$ heterostructures, a gate tunable superconducting electron gas is confined in a quantum well at the interface between two insulating oxides. Remarkably, the gas coexists with both magnetism and strong Rashba spin–orbit coupling. However, both the origin of superconductivity and the nature of the transition to the normal state over the whole doping range remain elusive. Here we use resonant microwave transport to extract the superfluid stiffness and the superconducting gap energy of the $LaAlO_3/SrTiO_3$ interface as a function of carrier density. We show that the superconducting phase diagram of this system is controlled by the competition between electron pairing and phase coherence. The analysis of the superfluid density reveals that only a very small fraction of the electrons condenses into the superconducting state. We propose that this corresponds to the weak filling of high-energy d_{xz}/d_{yz} bands in the quantum well, more apt to host superconductivity.

[1] Laboratoire de Physique et d'Etude des Matériaux, ESPCI Paris, PSL Research University, CNRS, 10 Rue Vauquelin, 75005 Paris, France. [2] Université Pierre and Marie Curie, Sorbonne-Universités, 75005 Paris, France. [3] Institute for Complex Systems (ISC-CNR), UOS Sapienza, Piazzale A. Moro 5, 00185 Roma, Italy. [4] Dipartimento di Fisica Università di Roma "La Sapienza", Piazzale A. Moro 5, 00185 Roma, Italy. [5] National Physical Laboratory, Council of Scientific and Industrial Research (CSIR), Dr. K.S. Krishnan Marg, New Delhi, 110012, India. [6] Condensed Matter Low Dimensional Systems Laboratory, Department of Physics, Indian Institute of Technology, Kanpur, 208016, India. [7] Unité Mixte de Physique CNRS-Thales, 1 Av. A. Fresnel, 91767 Palaiseau, France. G. Singh and A. Jouan contributed equally to this work. Correspondence and requests for materials should be addressed to L.B. (email: lara.benfatto@roma1.infn.it) or to N.B. (email: nicolas.bergeal@espci.fr)

The superconducting phase diagram of $LaAlO_3/SrTiO_3$ interfaces defined by plotting the critical temperature T_c as a function of electrostatic doping has the shape of a dome. It ends into a quantum critical point, where the T_c is reduced to zero, as carriers are removed from the interfacial quantum well[1–4]. Despite a few proposals[5–7], the origin of this carrier density dependence, and in particular the non-monotonic suppression of T_c, remains unclear. To investigate this issue, one must consider the two fundamental energy scales associated with superconductivity. On the one hand, the gap energy Δ measures the pairing strength between electrons that form Cooper pairs. On the other hand, the superfluid stiffness J_s determines the cost of a phase twist in the superconducting condensate. In conventional superconductors, well described by Bardeen–Cooper–Schrieffer (BCS) theory, J_s is much higher than Δ and the superconducting transition is controlled by the breaking of Cooper pairs. However, when the stiffness is strongly reduced, phase fluctuations play a major role and the suppression of T_c can be dominated by the loss of phase coherence[8]. Tunneling experiments in the low doping regime of $LaAlO_3/SrTiO_3$ interfaces evidenced the presence of a pseudogap in the density of states above T_c[9]. This can be interpreted as the signature of pairing surviving above T_c while superconducting coherence is destroyed by strong phase fluctuations, enhanced by a low superfluid stiffness[10]. Superconductor-to-insulator quantum phase transitions driven by gate voltage[1] or magnetic field[11] also highlighted the predominant role of phase fluctuations in the suppression of T_c.

The two-dimensional (2D) superfluid density derived from the stiffness $\left(n_s^{2D} = \frac{4m}{\hbar^2} J_s\right)$ has to be analyzed within the context of the peculiar $LaAlO_3/SrTiO_3$ band structure. Under strong quantum confinement, the degeneracy of the t_{2g} bands of $SrTiO_3$ (d_{xy}, d_{xz}, and d_{yz} orbitals) is lifted, generating a rich and complex band structure[12,13]. The emergence of superconductivity for a given carrier density suggests that it could be intrinsically related to orbital occupancy in the interfacial quantum well. Experiments performed on (110)-oriented $LaAlO_3/SrTiO_3$ interfaces, for which the ordering of the t_{2g} bands is reversed from that of the conventional (001) orientation, revealed that superconductivity behaves differently[14]. Instead of following the usual dome shape and disappearing at low doping, T_c is only weakly affected by gating over a wide range of carrier density. This shows the important role of orbitals ordering and also suggests that only some specific bands could host superconductivity[15]. In particular, it has been emphasized that the d_{xz}/d_{yz} band lying at high energy in the quantum well could play an important role because of its large density of states[6,7].

Here we use resonant microwave transport to measure the complex conductivity of the superconducting (001)-oriented $LaAlO_3/SrTiO_3$ interfaces. This allows us to directly extract the evolution of the superfluid stiffness in the phase diagram that we also convert into a gap energy through BCS theory in the dirty limit. Both energy scales are compared with theoretical predictions. The superfluid density n_s deduced from J_s is found to be close to the carrier density of the d_{xz}/d_{yz} band extracted from multiband Hall effect measurements, highlighting the key role of this band in the emergence of superconductivity.

Results

Resonant microwave transport experiment. In superconducting thin films, J_s is usually assessed either from penetration depth measurements[16,17] or from dynamic transport measurements[18,19]. This latter method was adapted in this work for the specific case of $LaAlO_3/SrTiO_3$ samples. While superconductors have an infinite dc conductivity, they exhibit a finite complex conductivity $\sigma(\omega)$ at non-zero frequency, which in 2D translates into a sheet conductance $G(\omega) = G_1(\omega) - iG_2(\omega)$. The real part $G_1(\omega)$ accounts for the transport of unpaired electrons existing at $T \neq 0$ and $\omega \neq 0$, and the imaginary part $G_2(\omega)$ accounts for the transport of Cooper pairs[20,21]. In the low-frequency limit $\hbar\omega \ll \Delta$, a superconductor behaves essentially as an inductor and $G_2(\omega) = \frac{1}{L_k\omega}$, where L_k is the kinetic inductance of the superconductor due to the inertia of Cooper pairs[22]. The superfluid stiffness is directly related to the inductive response of the condensate through the relation $J_s = \frac{\hbar^2}{4e^2 L_k}$.

In this study, 8-uc-thick $LaAlO_3$ epitaxial layers were grown on 3×3 mm^2 TiO_2-terminated (001) $SrTiO_3$ single crystals by pulsed laser deposition (see Methods section). After the growth, a weakly conducting metallic back-gate of resistance ~100 kΩ is deposited on the backside of the 200-μm- thick substrate. Figure 1 gives a schematic description of our experimental setup, inspired by recent developments in the field of quantum circuits[23,24]. The $LaAlO_3/SrTiO_3$ heterostructure is inserted in a microwave circuit board, between the central strip of a coplanar waveguide guide (CPW) transmission line and its ground. It is embedded into an RLC resonant circuit whose inductor L_1 and resistor R_1 are surface mounted microwave devices (SMDs), and whose capacitor C_{STO} is due to the substrate in parallel with the 2D electron gas (2-DEG) (Fig. 1a, c). Because of the high dielectric constant of $SrTiO_3$ at low temperature (i.e., $\epsilon_r \simeq 24{,}000$), C_{STO} dominates the circuit capacitance. More information on the sample environment can be found in the Supplementary Note 1 and Supplementary Fig. 1. A directional coupler is used to guide the microwave signal from port 1 to the sample through a bias-tee, and to separate the reflected signal which is amplified by a low-noise cryogenic high electron mobility transistor amplifier before reaching port 2 (Fig. 1b). The complex transmission coefficient $S_{21}(\omega)$ between the two ports is measured with a vector network analyzer. Standard microwave network analysis relates the reflection coefficient of the sample circuit $\Gamma(\omega)$ to $S_{21}(\omega)$ through complex error coefficients, which are determined by a calibration procedure (see Methods section and Supplementary Fig. 5). For a transmission line terminated by a circuit load of impedance $Z_L(\omega)$[25]

$$\Gamma(\omega) = \frac{A^{out}(\omega)}{A^{in}(\omega)} = \frac{Z_L(\omega) - Z_0}{Z_L(\omega) + Z_0}, \quad (1)$$

where A^{in} and A^{out} are the complex amplitudes of incident and reflected waves, and $Z_0 = 50\ \Omega$ is the characteristic impedance of the CPW transmission line. A reflection measurement gives therefore a direct access to the load impedance $Z_L(\omega)$ or equivalently its admittance $G_L(\omega) = 1/Z_L(\omega)$, commonly called complex conductance. In the present case, $Z_L(\omega)$ is the impedance of the RLC circuit represented in Fig. 1c, whose resonance frequency ω_0 in the superconducting state is directly related to the kinetic inductance of the 2-DEG. Measuring ω_0 as a function of gate voltage provides therefore a very direct method to determine the superfluid stiffness in the phase diagram. In addition, the setup of Fig. 1, which includes a bias-tee and protective capacitors in series with L_1 and R_1, allows measuring both the dc and ac microwave transport properties of the 2-DEG at the same time.

Resonance in the normal and superconducting states. After cooling the sample to 450 mK, the back-gate voltage is first swept to its maximum value +50 V while keeping the 2-DEG at the electrical ground, to ensure that no hysteresis will take place upon further gating[26]. In the limit $\omega \ll \tau^{-1}$ (τ is the elastic scattering time) and for temperatures higher than T_c, the 2-DEG behaves as

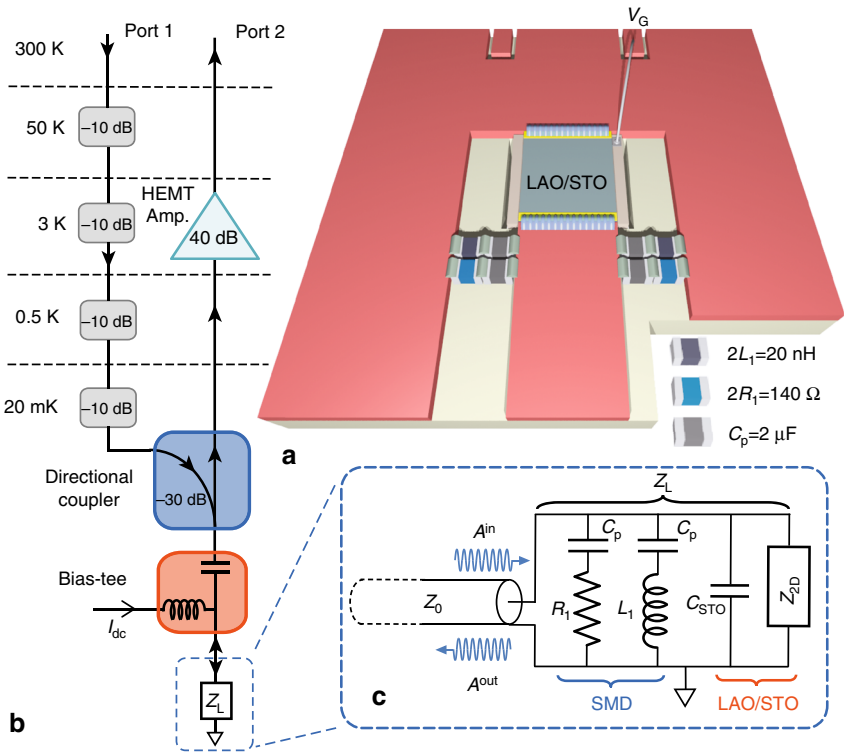

Fig. 1 The $LaAlO_3/SrTiO_3$ sample and its microwave measurement setup. **a** $LaAlO_3/SrTiO_3$ sample inserted between the central strip and the ground of a CPW transmission line, in parallel with SMD inductors L_1 and resistors R_1. C_p are protective capacitors that avoid dc current to flow through L_1 and R_1 without affecting ω_0. **b** Sample circuit of impedance Z_L in its microwave measurement set-up that includes an attenuated input line and an amplified readout line separated by a directional coupler. A bias-tee allows dc biasing of the sample. **c** Equivalent electrical circuit of the sample circuit including the SMDs and the $LaAlO_3/SrTiO_3$ heterostructure modeled by an impedance Z_{2D} in parallel with a capacitor C_{STO}. The reflection coefficient $\Gamma(\omega)$, taken at the discontinuity between the CPW line and the sample circuit, is defined as the ratio of the complex amplitude of the reflected wave $A^{out}(\omega)$ to that of the incident wave $A^{in}(\omega)$

a metal whose Drude conductance is simply the inverse of the dc resistance (Fig. 2c). The circuit displays a resonance at frequency $\omega_0 = \frac{1}{\sqrt{L_1 C_{STO}}}$. When $\omega \simeq \omega_0$, Z_L becomes purely real and the microwave signal is dissipated in the sample circuit. As a result, an absorption dip is observed in $\Gamma(\omega)$ along with a 2π phase shift (Fig. 2b). ω_0 varies upon gating because of the electric-field-dependent $SrTiO_3$ dielectric constant[27] (Fig. 2a). Thus, the deduced substrate capacitance, C_{STO}, decreases with the absolute value of the gate voltage (Fig. 2c). Note that C_{STO} also includes a small contribution due to the circuit parasitic capacitance (≃3.5 pF) (see Methods section and Supplementary Fig. 2). According to the geometry of the sample, its value at $V_G = 0$ V corresponds to a dielectric dielectric constant $\epsilon_r \simeq 23{,}700$ (Supplementary Fig. 3). In the superconducting state, the 2-DEG conductance acquires an imaginary part $G_2(\omega) = \frac{1}{L_k(T)\omega}$ that modifies ω_0, since the total inductance of the circuit is now $\frac{L_1 L_k(T)}{L_1 + L_k(T)}$ (L_1 in parallel with $L_k(T)$). The superconducting transition observed in dc resistance for positive gate voltages, V_G, coincides with a shift of ω_0 towards high frequency (Fig. 3b–d). We emphasize that this shift can already be detected in the uncalibrated $S_{21}(\omega)$ coefficient (Supplementary Fig. 4). In the absence of superconductivity (for $V_G < 0$ V), the resonance frequency remains unchanged as C_{STO} has no temperature dependence in the range of interest (Fig. 3a). In this experiment, the typical microwave current flowing into the sample circuit is <5 nA, which is much lower than the critical current of the superconducting 2-DEG (≃5 μA).

Superfluid stiffness and gap energy. In the following, we determine the gate dependence of the important energy scales in superconducting $LaAlO_3/SrTiO_3$ interfaces, and compare them with the BCS theory predictions. In Fig. 4a, we plot the gate dependence of the experimental superfluid stiffness $J_s^{exp} = \frac{\hbar^2}{4e^2 L_k}$ extracted from L_k at the lowest temperature $T = 20$ mK (≃0 K in the following). On the same logarithmic scale, we also show the gate dependence of the superconducting T_c defined as the temperature where $R_{dc} = 0\,\Omega$. The accuracy in the determination of the superfluid stiffness is limited by the uncertainty on the exact value of the circuit inductance L_1 and the contribution of the sample geometrical inductance. The total error, corresponding to the gray outline on Fig. 4a, is estimated to be lower than 15% for all gate voltages (Supplementary Note 2).

The superconducting 2-DEG is in the dirty limit in which the elastic scattering time τ is much shorter than the superconducting gap $\Delta(T=0)$ ($\frac{\Delta(0)\tau}{\hbar} \simeq 5.5 \times 10^{-3}$). Within this limit and for $\omega \ll \Delta(0)/\hbar$, the zero-temperature superfluid stiffness of a single-band BCS superconductor can be expressed as a function of $\Delta(0)$[28]:

$$J_s(0) = \frac{\pi\hbar}{4e^2 R_n} \cdot \Delta(0), \qquad (2)$$

where $R_n = R_{dc}(450\,mK)$ is the normal state resistance (Fig. 2c) that accounts for the reduction of stiffness because of scattering.

J_s^{exp} increases continuously with gate voltage in the entire phase diagram in agreement with a previous report[10]. Moreover, a remarkable agreement is obtained between experimental data $\left(J_s^{exp}\right)$ and BCS prediction (J_{BCS}) in the overdoped (OD) regime defined by $V_G > V_G^{opt} \simeq 27$ V, assuming a gap energy $\Delta(0) = 1.76 k_B T_c$ in Eq. (2) (Fig. 4a). In this regime, the superfluid stiffness J_s^{exp} takes a value much higher than T_c in agreement with

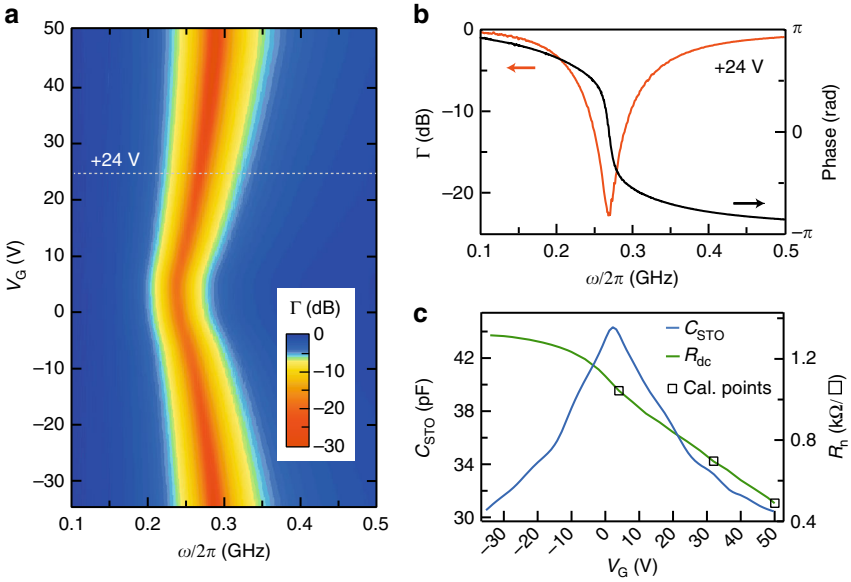

Fig. 2 Resonance of the sample circuit in the normal state at $T = 450$ mK. **a** Magnitude of $\Gamma(\omega)$ in dB (color scale) as a function of ω and V_G. **b** Magnitude and phase of $\Gamma(\omega)$ at $V_G = +24$ V. **c** Capacitance C_{STO} extracted from the resonance frequency $\omega_0 = 1/\sqrt{L_1 C_{STO}}$ (left axis) and normal dc resistance R_n (right axis) as a function of V_G. Square symbols indicate the values of V_G used for calibration

the BCS paradigm. However, in the underdoped (UD) regime, corresponding to $V_G < V_G^{opt}$, a discrepancy between the data and the BCS calculation is observed. The superfluid stiffness J_s^{exp} drops significantly while T_c and J_{BCS} evolve smoothly before vanishing only when approaching closely the quantum critical point where $T_c \simeq 0$ K ($V_G = 4$ V). This indicates that the loss of phase coherence of the superconducting condensate is stronger than what expected taking into account conventional scattering by defects, as encoded in Eq. (2). Such a behavior can then be ascribed to strong phase fluctuations probably reinforced by the presence of spatial inhomogeneities which has been proposed as an explanation for the observed broadening of the superconducting transitions[29,30]. In this context, it was shown that the 2-DEG in $LaAlO_3/SrTiO_3$ interfaces exhibits a behavior similar to the one of a Josephson junction array consisting of superconducting islands coupled through a metallic 2-DEG[11,31]. Whereas in the OD regime the islands are robust and tightly connected at $T \simeq 0$ K (homogeneous-like), in the UD regime, the charge carrier depletion makes the array more dilute. In this case, the system can maintain a rather high T_c ($R_{dc} = 0\ \Omega$) as long as the dc current can follow a percolating path through islands. However, the macroscopic stiffness J_s^{exp} is suppressed by phase fluctuations between islands and is therefore lower than that expected in a homogenous system of similar T_c.

We now convert J_s^{exp} into a superconducting gap energy Δ_s^{exp} through Eq. (2) (Fig. 4b). Strikingly, these two characteristic energy scales of superconductivity evolve quite differently with doping. While J_s^{exp} continuously increases with V_G (Fig. 4a), Δ_s^{exp} has a dome-shaped dependence (Fig. 4b). More precisely, in the OD regime, Δ_s^{exp} coincides with $1.76 k_B T_c$, and decreases like T_c while the superfluid stiffness increases: this is a clear indication that in this regime T_c is controlled by the pairing energy as in the BCS scenario. The maximum energy gap at optimal doping ($V_G^{opt} \simeq 27$ V) is $\Delta_s^{exp} \simeq 23$ μeV. This is in agreement with the BCS gap identified recently by Stornaiuolo et al.[32] at optimal doping using spectroscopic Josephson junctions in $LaAlO_3/SrTiO_3$ interfaces of similar T_c. By using tunneling spectroscopy on planar Au/$LaAlO_3/SrTiO_3$ junctions, Richter et al.[9] have reported an energy gap in the density of states of ≃40 μeV for optimally doped $LaAlO_3/SrTiO_3$ interfaces of higher T_c. In spite of this significantly higher gap energy, this corresponds to a $\frac{\Delta}{k_B T_c}$ ratio of 1.7, similar to our result. In the OD regime, we also checked that the gap value extracted from a BCS fit of the temperature dependence of J_s^{exp} matches Δ_s^{exp} obtained by Eq. (2) (Supplementary Note 3 and Supplementary Fig. 6). In the UD regime of the phase diagram, Δ_s^{exp} departs from $1.76 k_B T_c$ which is in contradiction with BCS theory. This behavior is also different from that of the tunneling gap which was found to increase in the UD regime[9]. In addition, a pseudogap has been observed above T_c in this regime, as also reported in high-T_c superconducting cuprates[33,34] or in strongly disordered films of conventional superconductors[28,35,36]. The results obtained by the two experimental approaches can be reconciled by considering carefully the measured quantities. In our case, the superconducting gap Δ_s^{exp} probed by microwaves is directly converted from the stiffness of the superconducting condensate and is therefore only reflective of the presence of a true phase-coherent state. On the other hand, tunneling experiments probe the single particle density of states, and can evidence pairing even without phase coherence. The two experimental methods provide complementary informations which indicate that in the UD region of the phase diagram, the superconducting transition is dominated by phase coherence rather than by electron pairing. In this case, the energy gap cannot be extracted from Eq. (2), which is valid only for BCS superconductors. Notice that in the low carrier density region corresponding to $V_G < 0$, some non-connected superconducting islands could already form without contributing to the macroscopic stiffness of the 2-DEG. Recently, preformed electron pairs without phase coherence has also been evidenced in $SrTiO_3$-based nanostructures raising the question of a possible Bose–Einstein condensation mechanism where pairing precedes the formation of the superconducting state[37].

Multiband transport. A simplified scheme of the band structure in the interfacial quantum well is presented in Fig. 5a, b[38]. The degeneracy of the three t_{2g} bands is lifted by the confinement in the z direction, leading to a splitting that is inversely proportional to the effective masses m_z along this direction. d_{xy} subbands are isotropic in the interface plane with an effective mass $m_{xy} = 0.7 m_0$,

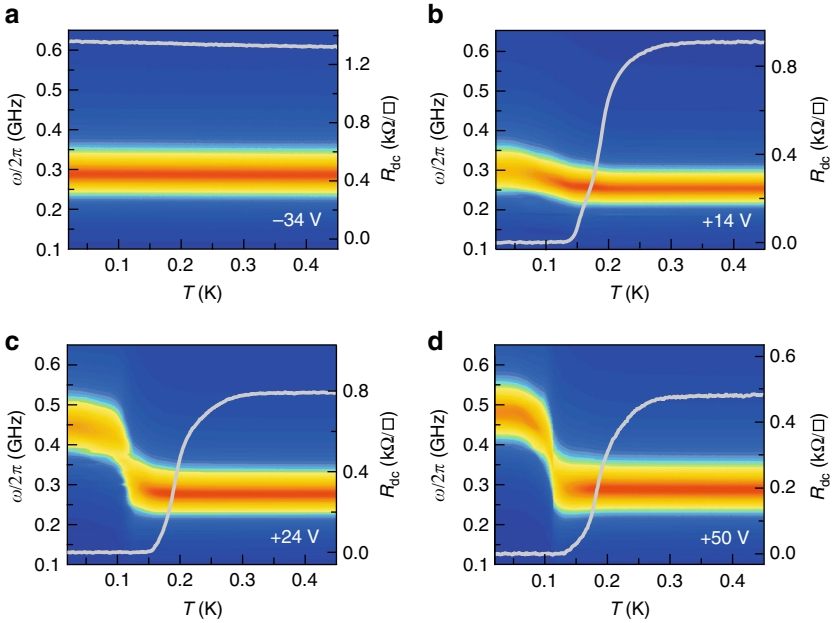

Fig. 3 Resonance of the sample circuit in the superconducting state. Magnitude of $\Gamma(\omega)$ in dB (color scale) as a function of frequency and temperature for the selected gate values, $V_G = -34$ V (**a**), $V_G = +14$ V (**b**), $V_G = +24$ V (**c**), and $V_G = +50$ V (**d**). The corresponding dc resistance as a function of temperature is shown in gray solid lines (right axis)

whereas the d_{xz}/d_{yz} bands are anisotropic with a corresponding average mass $m_{xz/yz} = \sqrt{m_x m_y} \simeq 3.13 m_0$. At low carrier densities, we expect several d_{xy} subbands to be populated, whereas at higher density ($V_G > 0$ V), the Fermi energy should enter into the d_{xz}/d_{yz} bands. Multiband transport in $LaAlO_3/SrTiO_3$ and $LaTiO_3/SrTiO_3$ interfaces has been observed experimentally in various magneto-transport experiments including quantum oscillations[39,40], magneto-conductance[15,41], and Hall effect[2,3,42–44]. Yang et al. [39] recently showed that, in addition to a majority of low-mobility carriers (LMCs), a small amount of high-mobility carriers (HMCs) is also present, with an effective mass close to the $m_{xz/yz}$ one. Despite a band mass substantially higher than the m_{xy} one, these carriers acquire a high mobility since $d_{xz/yz}$ orbitals extend deeper in $SrTiO_3$ where they recover bulk-like properties, including reduced scattering, higher dielectric constant and better screening. In Hall effect measurements, the Hall voltage is linear in magnetic field B in the low doping regime corresponding to one-band transport, but this is not the case at high doping because of the contribution of a new type of carriers (the HMC)[3]. We performed a two-band analysis of the Hall effect data combined with gate capacitance measurements to determine the contribution of the two populations of carriers to the total density n_{tot} (Fig. 5c)[3]. The first clear signature of multiband transport is seen when the Hall carrier density n_{Hall}, measured in the limit $B \to 0$, drops with V_G instead of following the charging curve of the gate capacitance (n_{tot} in Fig. 5d). Figure 5d, e show that LMC of density n_{LM} are always present, whereas a few HMC of density n_{HM} are injected in the 2-DEG for positive V_G, which corresponds to the region of the phase diagram where superconductivity is observed. In consistency with quantum oscillations measurements, we identify the LMC and the HMC as coming from the d_{xy} and d_{xz}/d_{yz} bands, respectively, and we emphasize that the addition of HMC in the quantum well triggers superconductivity.

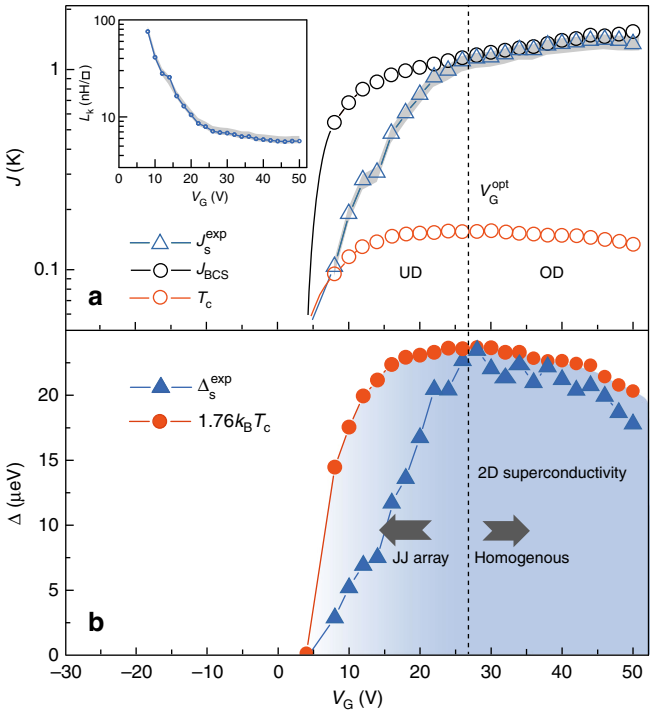

Fig. 4 Superfluid stiffness and phase diagram. **a** Experimental superfluid stiffness $J_s^{exp}(T \simeq 0)$ (open triangles) as a function of V_G compared with T_c taken at $R_{dc} = 0\ \Omega$ (red open circles), and with the BCS theoretical stiffness J_{BCS} expected from Eq. (2) assuming $\Delta(0) = 1.76 k_B T_c$ (black open circles). The gray outline indicate the total error margin in the determination of $J_s^{exp}(T \simeq 0)$. Inset) $L_k(T \simeq 0)$ as a function of V_G and error margin (gray outline). **b** Superfluid stiffness converted into a gap energy $\Delta_s^{exp}(T \simeq 0)$ as a function of V_G (plain triangles) compared with the expected BCS gap energy $1.76 k_B T_c$ (plain circles)

Discussion

To further outline the relation between HMC and superconductivity, we extract the superfluid density n_s^{2D} from J_s^{exp}

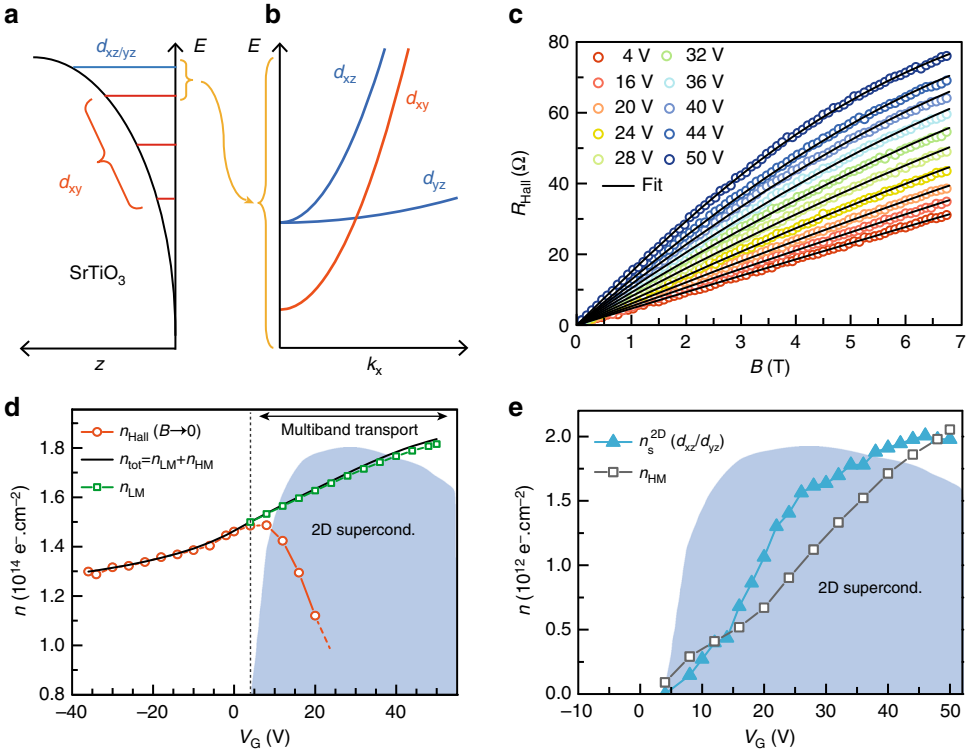

Fig. 5 Superfluid density and Hall effect analysis. **a** Scheme of the interfacial quantum well showing the splitting of the t_{2g} bands. **b** Simplified scheme of the band structure taking into account only the last filled d_{xy} subband, the d_{xz} band, and the d_{yz} band. **c** Hall resistance as a function of magnetic field for different $V_G > 0$ (open circles), fitted by at two-band model (black solid lines) (see Methods). **d** Hall carrier density $n_{Hall} = \frac{B}{eR_{Hall}}$ extracted in the limit $B \to 0$ (red open circles) and LMC density n_{LM} extracted from the two-band analysis (green open squares). The total carrier density n_{tot} is obtained by matching the charging curves of the gate capacitance with n_{Hall} at negative V_G (black solid line). The unscaled T_c dome in the background indicates the region where superconductivity is observed. **e** Superfluid density n_s^{2D} calculated from J_s^{exp} using a mass $m_{xz/yz}$ (plain triangles), compared with the HMC density n_{HM} (open squares)

assuming a mass $m_{xz/yz}$ for the electrons, and plot it as a function of the gate voltage (Fig. 5e). It increases continuously to reach $n_s^{2D} \simeq 2 \times 10^{12}\, e^-\,\mathrm{cm}^{-2}$ at maximum doping, which is approximately 1% of the total carrier density. The comparison of n_s^{2D} with n_{HM} shows that, unexpectedly, both quantities have a very similar dependence with the gate voltage and almost coincide numerically (Fig. 5e). This suggests that the emergence of the superconducting phase is mainly related to the filling of d_{xz}/d_{yz} bands, whose high density of states is favorable to superconductivity. Nevertheless, in the presence of interband coupling, superconductivity may also be induced in some d_{xy} subbands which would then slightly contribute to the total superfluid density.

Bert et al.[10] measured the superfluid density in $LaAlO_3/SrTiO_3$ interfaces using a scanning SQUID technique. The overall gate dependence is similar in both experiments, including in the OD regime where the superfluid density keeps increasing while T_c is reduced. However, in our case n_s^{2D} is lower despite a much higher carrier density ($n \simeq 1.8 \times 10^{14} e^-\,\mathrm{cm}^{-2}$ at maximum doping) which corresponds to the upper limit of the doping range commonly observed in $LaAlO_3/SrTiO_3$ interfaces. The fact that $n_s^{2D} \simeq n_{HM}$ may be somewhat intriguing as the dirty limit that we used in Eq. (2) implies that n_s^{2D} should correspond to a fraction of the total normal carrier density and not to n_{HM}. To clarify this situation, it is needed to go beyond single-band superconductor models that cannot account correctly for the unusual t_{2g}-based interfacial band structure of $LaAlO_3/SrTiO_3$ interfaces. Further investigations of recent experimental[45] and theoretical[46] developments on superconductors having two dissimilar bands (e.g., clean and dirty, weak, and strong coupling) should provide the starting framework to address this question.

In summary, we have measured the superfluid stiffness J_s of $LaAlO_3/SrTiO_3$ interfaces by implementing a resonant microwave transport experiment. Whereas a good agreement with the BCS theory is observed at high carrier doping, we find that the suppression of T_c at low doping is controlled by the loss of macroscopic phase coherence instead of electron pairing strength as in standard BCS theory. The corresponding superfluid density represents only a small fraction of the total electrons density. We emphasize here that the monotonic raise of n_s^{2D} with gate voltage indicates that the decrease of T_c in the OD region of the phase diagram cannot be attributed to a loss of superfluid density. The gate dependence of n_s^{2D} agrees qualitatively with the density of HMCs extracted from multiband Hall effect. We therefore propose that the emergence of superconductivity upon gating is related to the weak filling of the d_{xz}/d_{yz} bands taking place at higher energy in the quantum well. In addition to having a larger density of states, these d_{xz}/d_{yz} bands also extends much deeper in the substrate due to their out-of-plane mass. Away from the interface, the dielectric constant, which is most probably a fundamental ingredient for electron pairing[47], is less affected by the interfacial electric field and therefore closer to its nominal value. These delocalized electrons therefore recover properties similar to the ones found in bulk $SrTiO_3$, including BCS superconductivity[48]. Our finding is consistent with the observation of a gate-independent superconductivity in (110)-oriented $LaAlO_3/SrTiO_3$ interfaces for which the d_{xz}/d_{yz} bands have a lower energy than the d_{xy} subbands and are therefore always filled[14].

Methods

Sample growth. In this study, we used 8-uc-thick $LaAlO_3$ epitaxial layers grown on 3×3 mm^2 TiO_2-terminated (001) $SrTiO_3$ single crystals by pulsed laser deposition. The substrates were treated with buffered hydrofluoric acid to expose TiO_2-terminated surface. Before deposition, the substrate was heated to 830 °C for 1 h in an oxygen pressure of 7.4×10^{-2} mbar. The thin film was deposited at 800 °C in an oxygen partial pressure of 1×10^{-4} mbar. The $LaAlO_3$ target was ablated with a KrF excimer laser at a rate of 1 Hz with an energy density of 0.56–0.65 J cm^{-2}. The film growth mode and thickness were monitored using reflection high-energy electron diffraction (STAIB, 35 keV) during deposition. After the growth, a weakly conducting metallic back-gate of resistance ~100 kΩ (to avoid microwave shortcut of the 2-DEG) is deposited on the backside of the 200-µm-thick $SrTiO_3$ substrate.

Calibration procedure. In this experiment, the resonance frequency shift and correspondingly J_s can be extracted directly from the raw measurements of S_{21} in most of the regions of the phase diagram (Supplementary Fig. 4). Nevertheless, a calibration procedure can be applied to relate S_{21} measured with the Vector Network Analyzer to the reflection coefficient $\Gamma = (Z_L - Z_0)/(Z_L + Z_0)$ of the sample circuit. This procedure also suppresses parasitic signals mainly due to wave interferences in the microwave setup, and improves the precision on the measurement as illustrated in Supplementary Fig. 4b. The microwave setup can be modeled using the scattering matrix formalism as shown in Supplementary Fig. 5. The relation between the transmission coefficient between port 1 and port 2 $S_{21}(\omega)$ and the reflection coefficient of the sample circuit $\Gamma(\omega)$ is given by

$$S_{21} = \gamma + \frac{\alpha' \Gamma}{1 - \delta \Gamma}, \quad (3)$$

where $\alpha' = \alpha\beta$, γ, and δ are three error complex coefficients. They can be determined using three known values of $\Gamma = (Z_L - Z_0)/(Z_L + Z_0)$ which are obtained by imposing three different impedances Z_L. It is customary to use an open, a short, and a matched load as standard impedances to calibrate microwave setup. However, such method is neither adapted to our very low temperature experiment nor to our sample circuit geometry. Instead, our setup was calibrated by directly varying the impedance Z_L of the sample circuit with gate value. The main advantage of this method is that it fully takes into account the local microwave environment of the sample. The gate controls both the normal resistance of the 2-DEG whose value can be measured in dc and C_{STO} which can be extracted from ω_0. In practice, we choose a set of three gate values which correspond to well-separated resonance frequencies. Other sets allow the accuracy of the calibration to be checked. Supplementary Fig. 4 shows a comparison between the raw measurement of S_{21} and the corresponding calibrated Γ coefficient both in the normal state and the superconducting state for $V_G = 50$ V.

$SrTiO_3$ dielectric constant. The dielectric constant of the $SrTiO_3$ substrate can be retrieved from the value of C_{STO} plotted in Fig. 2c of the main text. For that, we performed numerical simulation using finite element method. We consider a 200-µm-thick 3×3 $SrTiO_3$ substrate covered by two 100-µm-wide Au/Ti strips as represented in Supplementary Fig. 1. Supplementary Fig. 4a shows the distribution of the electrostatic potential when one volt is applied on one Au/Ti strip while the other one is at the ground. Arrows indicate the direction of the electric field. The numerical simulation provides the corresponding capacitance between the two Au/Ti strips for a given dielectric constant ϵ_r. The gate dependence of ϵ_r that corresponds to the value of $(C_{STO} - C_{para})$ measured experimentally is shown in Supplementary Fig. 4b. At $V_G = 0$ V, $\epsilon_r \simeq 23{,}700$, which is consistent with the value found in the literature[27].

Multiband Hall effect and gate capacitance. The dependence of the total carrier density n_{tot} with V_G is obtained by integrating the gate capacitance $C(V_G)$, measured by standard lock-in technique, over the gate voltage range

$$n_{tot}(V_G) = n_{tot}(V_G = -36\,\mathrm{V}) + \frac{1}{eA}\int_{-36}^{V_G} C(V)\mathrm{d}V, \quad (4)$$

where A is the area of the sample and $n_{tot}(V_G = -36\,\mathrm{V})$ is matched to n_{Hall} since in this low doping regime the Hall effect is linear in magnetic field (single-band transport). In the multiband transport regime corresponding to $V_G > 0$, the Hall resistance has been fitted with a two-band model

$$R_{Hall} = \frac{B}{e}\frac{\frac{n_1\mu_1^2}{1+\mu_1^2B^2} + \frac{n_2\mu_2^2}{1+\mu_2^2B^2}}{\left[\frac{n_1\mu_1}{1+\mu_1^2B^2} + \frac{n_2\mu_2}{1+\mu_2^2B^2}\right]^2 + \left[\frac{n_1\mu_1^2B}{1+\mu_1^2B^2} + \frac{n_2\mu_2^2B}{1+\mu_2^2B^2}\right]^2}, \quad (5)$$

where n_1 and n_2 are the 2D electron densities and, μ_1 and μ_2 the corresponding mobilities. Fits are performed with the two constraints: $n_{tot} = n_1 + n_2$ and $1/R_{dc} = e(n_1\mu_1 + n_2\mu_2)$. The two populations of electrons are then identified as the LMC and the HMC.

Data availability. All data that support the findings of this study are available from the corresponding authors upon request.

Received: 3 July 2017 Accepted: 8 January 2018
Published online: 29 January 2018

References

1. Caviglia, A. D. et al. Electric field control of the $LaAlO_3/SrTiO_3$ interface ground state. *Nature* **456**, 624–627 (2008).
2. Bell, C. et al. Dominant mobility modulation by the electric field effect at the $LaAlO_3/SrTiO_3$ interface. *Phys. Rev. Lett.* **103**, 226802 (2009).
3. Biscaras, J. et al. Two-dimensional superconductivity induced by high-mobility carrier doping in $LaTiO_3/SrTiO_3$ heterostructures. *Phys. Rev. Lett.* **108**, 247004 (2012).
4. Hurand, S. et al. Field-effect control of superconductivity and Rashba spin–orbit coupling in top-gated $LaAlO_3/SrTiO_3$ devices. *Sci. Rep.* **5**, 12751 (2015).
5. Maniv, E. et al. Strong correlations elucidate the electronic structure and phase diagram of $LaAlO_3/SrTiO_3$ interface. *Nat. Commun.* **6**, 8239 (2015).
6. Gariglio, S., Gabay, M. & Triscone, J.-M. Research update: conductivity and beyond at the $LaAlO_3/SrTiO_3$ interface. *APL Mater.* **4**, 060701 (2016).
7. Valentinis, D. et al. Modulation of the superconducting critical temperature due to quantum confinement at the $LaAlO_3/SrTiO_3$ interface. *Phys. Rev. B* **96**, 094518 (2017).
8. Emery, V. J. & Kivelson, S. A. Importance of phase fluctuations in superconductors with small superfluid density. *Nature* **374**, 434–437 (1994).
9. Richter, C. et al. Interface superconductor with gap behaviour like a high-temperature superconductor. *Nature* **502**, 528–531 (2013).
10. Bert, J. A. et al. Gate-tuned superfluid density at the superconducting $LaAlO_3/SrTiO_3$ interface. *Phys. Rev. B* **86**, 060503(R) (2012).
11. Biscaras, J. et al. Multiple quantum criticality in a two-dimensional superconductor. *Nat. Mater.* **12**, 542–548 (2013).
12. Salluzzo, M. et al. Orbital reconstruction and the two-dimensional electron gas at the $LaAlO_3/SrTiO_3$ Interface. *Phys. Rev. Lett.* **102**, 166804 (2009).
13. Berner, G. et al. Direct k-space mapping of the electronic structure in an oxide–oxide interface. *Phys. Rev. Lett.* **110**, 247601 (2013).
14. Herranz, G. et al. Engineering two-dimensional superconductivity and Rashba spin–orbit coupling in $LaAlO_3/SrTiO_3$ quantum wells by selective orbital occupancy. *Nat. Commun.* **6**, 6028 (2015).
15. Joshua, A., Pecker, S., Ruhman, J., Altman, E. & Ilani, S. A universal critical density underlying the physics of electrons at the $LaAlO_3/SrTiO_3$ interface. *Nat. Commun.* **3**, 1129 (2012).
16. Ganguly, R., Chaudhuri, D., Raychaudhuri, P. & Benfatto, L. Slowing down of vortex motion at the Berezinskii–Kosterlitz–Thouless transition in ultrathin NbN films. *Phys. Rev. B* **91**, 054514 (2015).
17. Zuev, Y., Kim, M. S. & Lemberger, T. R. Correlation between superfluid density and T_c of Underdoped $YBa_2Cu_3O_{6+x}$ near the superconductor-insulator transition. *Phys. Rev. Lett.* **95**, 137002 (2005).
18. Kitano, H., Ohashi, T. & Maeda, A. Broadband method for precise microwave spectroscopy of superconducting thin films near the critical temperature. *Rev. Sci. Instrum.* **79**, 074701 (2008).
19. Scheffler, M. & Dressel, M. Broadband microwave spectroscopy in Corbino geometry for temperatures down to 1.7 K. *Rev. Sci. Instrum.* **76**, 074702 (2005).
20. Mattis, C. & Bardeen, J. Theory of the anomalous skin effect in normal and superconducting metals. *Phys. Rev.* **111**, 412 (1958).
21. Dressel, M. Electrodynamics of Metallic Superconductors. *Adv. Condens. Matter Phys.* **2013**, 104379 (2013).
22. Tinkham, M. *Introduction to Superconductivity* 2nd edn (Dover, Mineola, NY, 2004).
23. Wallraff, A. et al. Strong coupling of a single photon to a superconducting qubit using circuit quantum electrodynamics. *Nature* **431**, 162–167 (2004).
24. Bergeal, N. et al. Phase-preserving amplification near the quantum limit with a Josephson ring modulator. *Nature* **465**, 64–68 (2010).
25. Pozar, D. M. *Microwave Engineering* 4th edn (Wiley, New York, NY, 2012).
26. Biscaras, J. et al. Limit of the electrostatic doping in two-dimensional electron gases of $LaXO_3$(X = Al,Ti)/$SrTiO_3$. *Sci. Rep.* **4**, 6788 (2014).
27. Neville, R. C., Hoeneisen, B. & Mead, C. A. Permittivity of strontium titanate. *J. Appl. Phys.* **43**, 2124 (1972).
28. Pracht, U. S. et al. Enhanced cooper pairing versus suppressed phase coherence shaping the superconducting dome in coupled aluminum nanograins. *Phys. Rev. B* **93**, 100503 (2016).
29. Caprara, S. et al. Multiband superconductivity and nanoscale inhomogeneity at oxide interfaces. *Phys. Rev. B* **88**, 020504(R) (2013).
30. Scopigno, N. et al. Phase separation from electron confinement at oxide interfaces. *Phys. Rev. Lett.* **116**, 026804 (2016).

31. Prawiroatmodjo, G. E. D. K. et al. Evidence of weak superconductivity at the room-temperature grown $LaAlO_3/SrTiO_3$ interface. *Phys. Rev. B* **93**, 184504 (2016).
32. Stornaiuolo, D. et al. Signatures of unconventional superconductivity in the $LaAlO_3/SrTiO_3$ two-dimensional system. *Phys. Rev. B* **95**, 140502(R) (2017).
33. Renner, C., Revaz, B., Genoud, J.-Y., Kadowaki, K. & Fischer, O. Pseudogap precursor of the superconducting gap in under- and overdoped $Bi_2Sr_2CaCu_2O_{8+\delta}$. *Phys. Rev. Lett.* **80**, 149 (1998).
34. Timusk, T. & Statt, B. The pseudogap in high-temperature superconductors: an experimental survey. *Rep. Prog. Phys.* **62**, 61–122 (1999).
35. Sacépé, B. et al. Pseudogap in a thin film of a conventional superconductor. *Nat. Commun.* **1**, 140 (2010).
36. Mondal, M. et al. Phase fluctuations in a strongly disordered s-wave NbN superconductor close to the metal-insulator transition. *Phys. Rev. Lett.* **106**, 047001 (2011).
37. Cheng, G. et al. Electron pairing without superconductivity. *Nature* **521**, 196–199 (2015).
38. Kim, Y., Lutchyn, R. M. & Nayak, C. Origin and transport signatures of spin–orbit interactions in one- and two-dimensional $SrTiO_3$ -based heterostructures. *Phys. Rev. B* **87**, 245121 (2013).
39. Yang, M. et al. High-field magneto-transport in two-dimensional electron gas $LaAlO_3/SrTiO_3$. *Appl. Phys. Lett.* **109**, 122106 (2016).
40. Ben Shalom, M., Ron, A., Palevski, A. & Dagan, Y. ShubnikovDe Haas oscillations in $SrTiO_3/LaAlO_3$ interface. *Phys. Rev. Lett.* **105**, 206401 (2010).
41. Fête, A., Gariglio, S., Caviglia, A. D., Triscone, J.-M. & Gabay, M. Rashba induced magnetoconductance oscillations in the $LaAlO_3$-$SrTiO_3$ heterostructure. *Phys. Rev. B* **86**, 201105(R) (2012).
42. Kim, J. S. et al. Nonlinear Hall effect and multichannel conduction in $LaTiO_3/SrTiO_3$ superlattices. *Phys. Rev. B* **82**, 201407 (2010).
43. Ohtsuka, R., Matvejeff, M., Nishio, N., Takahashi, R. & Lippmaa, M. Transport properties of $LaTiO_3/SrTiO_3$ heterostructures. *Appl. Phys. Lett.* **96**, 192111 (2010).
44. Singh, G. et al. Effect of disorder on superconductivity and Rashba spin–orbit coupling in $LaAlO_3/SrTiO_3$ interfaces. *Phys. Rev. B* **96**, 024509 (2017).
45. Dai, Y. M. et al. Coexistence of clean- and dirty-limit superconductivity in LiFeAs. *Phys. Rev. B* **93**, 054508 (2016).
46. Chubukov, A. V., Eremin, I. & Efremov, D. V. Superconductivity versus bound-state formation in a two-band superconductor with small Fermi energy: applications to Fe pnictides/chalcogenides and doped $SrTiO_3$. *Phys. Rev. B* **93**, 174516 (2016).
47. Edge, J. M., Kedem, Y., Aschauer, U., Spaldin, N. A. & Balatsky, A. V. Quantum critical origin of the superconducting dome in $SrTiO_3$. *Phys. Rev. Lett.* **115**, 247002 (2016).
48. Thiemann, M. et al. Single gap superconductivity in doped $SrTiO_3$. Preprint at https://arxiv.org/abs/1703.04716 (2017).

Acknowledgements

We acknowledge R. Lobo, C. Castellani, and J. Lorenzana for useful discussions. This work has been supported by the Région Ile-de-France in the framework of CNano IdF, OXYMORE, and Sesame programs, by CNRS through a PICS program (S2S) and ANR JCJC (Nano-SO2DEG). L.B. acknowledges financial support by the Italian MAECI under the Italian-India collaborative project SUPERTOP-PGR04879. Part of this work has been supported by the IFCPAR French-Indian program (contract 4704-A). Research in India was funded by the CSIR and DST, Government of India.

Author contributions

G. S. and A. J. performed the measurements assisted by N.B. Samples were fabricated by P.K. and E.L. under the supervision of A.D., R.C.B., A.B., and M.B. G.S., A.J., and N.B. carried out the analysis of the results and wrote the article with the help of L.B., M.B., and J.L. F.C., C.F.-P., A.B., M.G., and S.C. contributed to discussions of the results.

Additional information

Supplementary Information accompanies this paper at https://doi.org/10.1038/s41467-018-02907-8.

Competing interests: The authors declare no competing financial interests.

Reprints and permission information is available online at http://npg.nature.com/reprintsandpermissions/

Publisher's note: Springer Nature remains neutral with regard to jurisdictional claims in published maps and institutional affiliations.